V.H. Hall-Chen, F.I. Parra, J.C. Hillesheim, J. Ruiz Ruiz, N.A. Crocker, P. Shi, H.S. Chu, S.J. Freethy, L.A. Kogan, W.A. Peebles, Q.T. Pratt, T.L. Rhodes, K. Ronald, R. Scannell, D.C. Speirs, S. Storment, J. Trisno

Effect of mismatch on Doppler backscattering in MAST plasmas

Effect of mismatch on Doppler backscattering in MAST plasmas

V.H. Hall-Chen, F.I. Parra, J.C. Hillesheim, J. Ruiz Ruiz, N.A. Crocker, P. Shi, H.S. Chu, S.J. Freethy, L.A. Kogan, W.A. Peebles, Q.T. Pratt, T.L. Rhodes, K. Ronald, R. Scannell, D.C. Speirs, S. Storment, J. Trisno

Effect of mismatch on Doppler backscattering in MAST and MAST-U plasmas

V.H. Hall-Chen[1,2,3]**, F.I. Parra**[4]**, J.C. Hillesheim**[2]**, J. Ruiz Ruiz**[1]**, N.A. Crocker**[5]**, P. Shi**[2]**, H.S. Chu**[3]**, S.J. Freethy**[2]**, L.A. Kogan**[2]**, W.A. Peebles**[5]**, Q.T. Pratt**[5]**, T.L. Rhodes**[5]**, K. Ronald**[6]**, R. Scannell**[2]**, D.C. Speirs**[6]**, S. Storment**[5]**, J. Trisno**[3]

[1] Rudolf Peierls Centre for Theoretical Physics, University of Oxford, Oxford OX1 3PU, UK

[2] UKAEA/CCFE, Culham Science Centre, Abingdon, Oxon, OX14 3DB, UK

[3] Institute of High Performance Computing, Singapore 138632, Singapore

[4] Princeton Plasma Physics Laboratory, Princeton, NJ 08540, USA

[5] Department of Physics and Astronomy, University of California, Los Angeles, CA 90095, USA

[6] Department of Physics, SUPA, University of Strathclyde, Glasgow G4 0NG, UK

E-mail: `valerian_hall-chen@ihpc.a-star.edu.sg`

November 2022

Abstract. The Doppler backscattering (DBS) diagnostic, also referred to as Doppler reflectometry, measures turbulent density fluctuations of intermediate length scales, typically $10 \gtrsim k_\perp \rho_i \gtrsim 1$; here $k_\perp$ is the turbulence's wavenumber and ρ_i is the ion gyroradius. The backscattered power is proportional to the power of the turbulent fluctuations. However, when the beam's wavevector is not properly aligned perpendicular to the magnetic field, the backscattered power is attenuated. The extent to which one is misaligned is quantified by the mismatch angle, and the reduction in power is the associated mismatch attenuation. In previous work, we used a beam model to derive a quantitative dependence of the mismatch attenuation on the mismatch angle, and preliminary comparisons with the results from MAST and MAST-U were promising. In this article, we analyse MAST and MAST-U DBS for different frequency channels and at various times, demonstrating that the beam model can indeed quantitatively account for the mismatch attenuation. This is especially important for spherical tokamaks, since the pitch angle varies significantly both spatially and temporally.

1. Introduction

The Doppler backscattering (DBS) diagnostic, also referred to as Doppler reflectometry, measures flows [1, 2, 3, 4, 5, 6] and turbulent density fluctuations of intermediate length scales, typically $10 \gtrsim k_\perp \rho_i \gtrsim 1$ [7, 8]. Here $k_\perp$ is the turbulence's wavenumber and ρ_i is the ion gyroradius. Additionally, the DBS diagnostic is able to measure turbulence in

the core, which is challenging. It is also likely to enjoy continued usage in future fusion reactors, as it is robust enough to survive the high neutron fluxes involved [9, 10].

The diagnostic works as follows. A microwave beam is sent into the plasma, and the backscattered signal is measured by the same antenna that emits the probe beam. As such, the wavenumber of turbulence responsible for backscattering at any point along the beam's path is twice that of the beam's wavenumber. This is commonly known as the Bragg condition. Additionally, the wavevector of the turbulence has to be parallel to that of the beam. This condition is not always exactly met. The turbulence wavevector perpendicular to the magnetic field is much larger than that parallel to it, hence the beam wavevector has to also be perpendicular to the field. We call the angle between these two wavevectors the mismatch angle, and the associated decrease of the signal the mismatch attenuation. The mismatch angle attenuating DBS signals is a concern already raised by previous work [11, 12, 13, 14, 15, 16]. In addition to DBS, analogous wavevector mismatch is also important for the cross-polarisation scattering diagnostic [17] and the high-k scattering diagnostic [18].

DBS has been implemented at many tokamaks and stellarators [19, 20, 21, 22, 23, 24, 25, 26, 27, 28, 29, 30, 31, 32]. However, the analysis of the DBS signal is more complicated in spherical tokamaks, since the pitch angle is not only large, but also varies both temporally and spatially. Hence, if the DBS has multiple launch frequencies or if the equilibrium is changing throughout the shot, as was the case for the MAST DBS, it would not possible to optimise steering for all frequencies or at all times, respectively [12]. Even in the best of cases, most of the frequencies will have at least a significant mismatch attenuation most of the time. The need for a quantitative understanding of mismatch is more pressing, with MAST-U starting operations recently [33], NSTX-U hopefully beginning operations soon [34], and STEP planned for the future [35]. MAST-U will have two DBS systems, one from SWIP [36, 28], and the other from UCLA [37, 38, 32]. Similarly, NSTX-U will have a DBS diagnostic. Being able to correct for mismatch attenuation in these systems will enable us to properly characterise the turbulence in spherical tokamaks, which is interesting in itself for the rich physics involved, and will also help us design better spherical tokamaks in the future. Moreover, recent work [13, 15, 16] indicates that mismatch attenuation is significant even in conventional tokamaks; the same techniques demonstrated in this paper would also apply to them.

To evaluate our understanding of mismatch attenuation and thus our ability to account for it, we study a groups of repeated shots carried out at the Mega-Ampere Spherical Tokamak (MAST) [39] another on its upgrade, MAST-U. The first of these shot groups has previously been analysed with a heuristic estimate of the mismatch attenuation [12], and properly evaluated only at a single time [14, 16]. The second group has only been evaluated for a single frequency at a single time [16].

We begin by summarising relevant insights and the associated formalism from our previous work [14] on the beam model of DBS in Section 2. We then detail how experimental data is processed in Section 3. Next, we have the key results of this paper: we evaluate the effectiveness of the beam model in quantitatively accounting for

the mismatch attenuation in Section 4. We conclude in Section 5.

2. Summary of the beam model

We use the beam model of Doppler backscattering in [14] to account for the effect of mismatch, evaluating the applicability of the model to spherical tokamak plasmas. This model uses the reciprocity theorem [40, 41] in conjunction with beam tracing [42, 43], enabling us to evaluate the backscattered signal in general geometry.

To introduce notation, we briefly summarise said model over the rest of this section. We linearise the dielectric tensor, such that it has a large part associated with the equilibrium $\boldsymbol{\epsilon}_{eq}$ and a small part related to the turbulent density fluctuations $\boldsymbol{\epsilon}_{tb}$,

$$\boldsymbol{\epsilon}_{tb} = \frac{\delta n_e}{n_e}(\boldsymbol{\epsilon}_{eq} - \mathbf{1}).\tag{1}$$

Here $\mathbf{1}$ is the 3×3 identity matrix, while n_e and δn_e are equilibrium and fluctuating parts of the electron density, respectively. The two pieces of the dielectric tensor, $\boldsymbol{\epsilon}_{eq}$ and $\boldsymbol{\epsilon}_{tb}$, determine two distinct pieces of the microwave electric field: the beam electric field $\mathbf{E}_b$,

$$\frac{c^2}{\Omega^2}\nabla \times (\nabla \times \mathbf{E}_b) = \boldsymbol{\epsilon}_{eq} \cdot \mathbf{E}_b,\tag{2}$$

and the scattered electric field $\mathbf{E}_s$,

$$\frac{c^2}{\Omega^2}\nabla \times (\nabla \times \mathbf{E}_s) = \boldsymbol{\epsilon}_{tb} \cdot \mathbf{E}_b + \boldsymbol{\epsilon}_{eq} \cdot \mathbf{E}_s,\tag{3}$$

where c is the speed of light and Ω is the angular frequency of the probe beam. We use various diagnostics, such as Thomson scattering and Mirnov coils, to find $\boldsymbol{\epsilon}_{eq}$. With the equilibrium dielectric tensor, we use beam tracing to find the probe beam's electric field $\mathbf{E}_b$ and the reciprocity theorem [40, 41] to determine the relevant scattered electric field $\mathbf{E}_s$.

Beam tracing for fusion plasmas was developed some time ago [43, 44]. In this work, we use the formalism presented in Appendix A of our earlier work [14]. Beam tracing involves evolving a Gaussian beam along a central ray $\mathbf{q}(\tau)$, where τ is a scalar coordinate that determines the position along the ray. The probe beam's electric field is given by

$$\begin{aligned}\mathbf{E}_b = A_{ant} \exp(i\phi_G + i\phi_P) &\left[\frac{\det(\mathrm{Im}[\boldsymbol{\Psi}_w])}{\det(\mathrm{Im}[\boldsymbol{\Psi}_{w,ant}])}\right]^{\frac{1}{4}} \sqrt{\frac{g_{ant}}{g}}\\ &\times \hat{\mathbf{e}} \exp\left(is + i\mathbf{K}_w \cdot \mathbf{w} + \frac{i}{2}\mathbf{w} \cdot \boldsymbol{\Psi}_w \cdot \mathbf{w}\right).\end{aligned}\tag{4}$$

Here A_{ant} is the amplitude of the probe's electric field at the antenna, ϕ_G is the Gouy phase, ϕ_P is the phase associated with the changing polarisation when propagating through a plasma, $\hat{\mathbf{e}}$ is the polarisation of the beam, $\mathbf{g} = d\mathbf{q}/d\tau$ is the group velocity, $\mathbf{w}$ is the position vector perpendicular to the central ray, s is the eikonal, the complex symmetric matrix $\boldsymbol{\Psi}_w$ contains the beam width and curvature, and $\mathbf{K}$ is the wavevector

of the beam. The subscript $_{ant}$ denotes that the quantity is evaluated at the antenna, while $_w$ indicates that the quantity is projected in the direction perpendicular to the central ray of the beam, that is, in the $\mathbf{1} - \hat{\mathbf{g}}\hat{\mathbf{g}}$ direction, where $\hat{\mathbf{g}} = \mathbf{g}/g$. The eikonal is given by

$$s = \int_0^\tau K_g(\tau')g(\tau') \, \mathrm{d}\tau', \tag{5}$$

with $K_g(\tau) = \mathbf{K}(\tau) \cdot \hat{\mathbf{g}}(\tau)$ being the projection of the wavevector along the ray. In the orthonormal basis $(\hat{\mathbf{x}}, \hat{\mathbf{y}}, \hat{\mathbf{g}})$, the vectors $\mathbf{w}$ and $\mathbf{K}_w$, as well as the matrix $\boldsymbol{\Psi}_w$, are given by

$$\mathbf{w} = \begin{pmatrix} w_x \\ w_y \\ 0 \end{pmatrix}, \tag{6}$$

$$\mathbf{K}_w = \begin{pmatrix} K_x \\ K_y \\ 0 \end{pmatrix}, \tag{7}$$

and

$$\boldsymbol{\Psi}_w = \begin{pmatrix} \Psi_{xx} & \Psi_{xy} & 0 \\ \Psi_{yx} & \Psi_{yy} & 0 \\ 0 & 0 & 0 \end{pmatrix}. \tag{8}$$

The real part of $\boldsymbol{\Psi}_w$ is responsible for the curvature of the Gaussian beam, while its imaginary part gives the characteristic decay width of the Gaussian envelope. In general, the real and imaginary parts are not simultaneously diagonalisable. When separately diagonalised, the eigenvalues of the real part are

$$[\mathrm{Re}\,(\boldsymbol{\Psi}_w)]_{\alpha\alpha} = \frac{K^3}{K_g^2} \frac{1}{R_{b,\alpha}}, \tag{9}$$

where $R_{b,\alpha}$ are the principal radii of curvature of the beam front, while the eigenvalues of the imaginary part are

$$[\mathrm{Im}\,(\boldsymbol{\Psi}_w)]_{\alpha\alpha} = \frac{2}{W_\alpha^2}, \tag{10}$$

where W_α are the principal beam widths. We solve for $\mathbf{E}_b$, given in equation (4), with our in-house beam-tracing code, Scotty [14].

Once we determine the probe beam's electric field, we find the backscattered amplitude via reciprocity [40, 41],

$$A_r = \frac{\Omega\mathrm{i}}{2c} \int \mathbf{E}^{(+)} \cdot \boldsymbol{\epsilon}_{tb} \cdot \mathbf{E}_b \, \mathrm{d}V. \tag{11}$$

As it turns outs, for cold plasmas, the reciprocal electric field $\mathbf{E}^{(+)}$ has almost the same form as $\mathbf{E}_b$ [14]. To evaluate the integrals, we need to take into account the fact that

turbulence structures are elongated along the magnetic field. For this reason, we define an orthonormal basis $(\hat{\mathbf{u}}_1, \hat{\mathbf{u}}_2, \hat{\mathbf{b}})$ at each point along the beam, given by

$$\hat{\mathbf{u}}_1 = \frac{(\hat{\mathbf{b}} \times \hat{\mathbf{g}}) \times \hat{\mathbf{b}}}{|(\hat{\mathbf{b}} \times \hat{\mathbf{g}}) \times \hat{\mathbf{b}}|}, \tag{12}$$

and

$$\hat{\mathbf{u}}_2 = \frac{\hat{\mathbf{b}} \times \hat{\mathbf{g}}}{|\hat{\mathbf{b}} \times \hat{\mathbf{g}}|}. \tag{13}$$

We also associate another orthonormal basis $(\hat{\mathbf{x}}, \hat{\mathbf{y}}, \hat{\mathbf{g}})$ with each point along the beam to express the beam characteristics, and we align it with the $(\hat{\mathbf{u}}_1, \hat{\mathbf{u}}_2, \hat{\mathbf{b}})$ basis as shown in Figure 1. We choose $\hat{\mathbf{y}} = \hat{\mathbf{u}}_2$ and denote projection in that direction with the subscript y. The other basis which is perpendicular to both $\hat{\mathbf{g}}$ and $\hat{\mathbf{y}}$ is

$$\hat{\mathbf{x}} = \frac{\hat{\mathbf{y}} \times \hat{\mathbf{g}}}{|\hat{\mathbf{y}} \times \hat{\mathbf{g}}|} = \frac{\hat{\mathbf{u}}_2 \times \hat{\mathbf{g}}}{|\hat{\mathbf{u}}_2 \times \hat{\mathbf{g}}|}. \tag{14}$$

Refer to our previous work [14] for a more in-depth discussion of the coordinate systems used in the beam model.

To make analytical progress, we need to make a few assumptions about the mismatch angle. We consider two situations, the *small-mismatch* and *large-mismatch* orderings. These names refer to two different orderings typical of but not exclusive to conventional and spherical tokamaks, respectively. In the *small-mismatch* ordering, the mismatch angle is small throughout the path of the beam, $\theta_m \sim W/L$; the signal is largely localised to the cut-off location. This backscattered signal from the cut-off is attenuated by mismatch, which we determine with our model. In the *large-mismatch* ordering, the mismatch angle is allowed to be up to order unity along the path of the beam, but on at least one point along the beam, it must be zero. The signal is then localised to the points of zero mismatch, which may not be at the cut-off. We showed [14] that even in regimes that are moderately *large-mismatch*, the result obtained from the *small-mismatch* ordering are still applicable.

Consequently, we now consider the small mismatch angle limit. After several integrals across and along the beam, and in one of the directions of $\mathbf{k}_\perp$, equation (11) gives

$$\frac{p_r}{P_{ant}} = \frac{\sqrt{\pi^3}e^4}{2c^2\Omega^2\epsilon_0^2 m_e^2 \bar{W}_y} \int F_p \frac{g_{ant}^2}{g^2} \frac{\bar{W}_y \det\left[\mathrm{Im}\left(\boldsymbol{\Psi}_w\right)\right]}{\sqrt{2}\left|\det\left[\boldsymbol{M}_w\right]\right|\left[-\mathrm{Im}\left(M_{yy}^{-1}\right)\right]^{\frac{1}{2}}} \exp\left(-\frac{\theta_m^2}{(\Delta\theta_m)^2}\right) \tag{15}$$
$$\times \left\langle \delta n_e^2(t)\right\rangle_t \widetilde{C}_l(\omega) \, \mathrm{d}l,$$

where we have expressed the integral along the other direction of $\mathbf{k}_\perp$ as an integral along the arc length l of the central ray [14]. We introduce the notation in the rest of this section. Here p_r is the spectral density, l is the arc-length along the central ray, $\boldsymbol{M}_w$ is the symmetric modified $\boldsymbol{\Psi}_w$ matrix as given in Appendix A, and the shorthand

$$\widetilde{C}_l(\omega) = \widetilde{C}\left(\mathbf{r} = \mathbf{q}(\tau(l)), k_{\perp,1} = -2K(\tau(l)), k_{\perp,2} = 0, \Delta u_\parallel = 0, \omega\right) \tag{16}$$
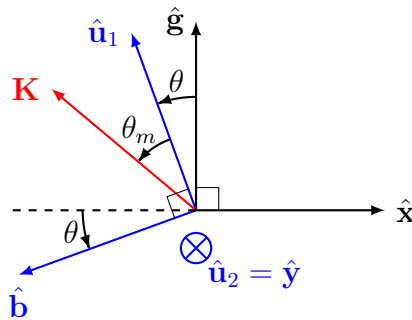
Figure 1: Bases for $\mathbf{k}_\perp$ and $\mathbf{w}$.

where $\widetilde{C}$ is the Fourier-transformed correlation function, given by

$$\widetilde{C}(\mathbf{r}, k_{\perp,1}, k_{\perp,2}, \Delta u_\parallel, \omega)$$

$$= \langle \delta n_e^2(\mathbf{r}, t) \rangle_t^{-1} \int \delta \tilde{n}_e \left(k_{\perp,1}, k_{\perp,2}, u_\parallel + \Delta u_\parallel, \omega \right) \delta \tilde{n}_e^* \left(k'_{\perp,1}, k'_{\perp,2}, u_\parallel, \omega \right) \tag{17}$$

$$\times \exp \left[i(k_{\perp,1} - k'_{\perp,1})u_1 + i(k_{\perp,2} - k'_{\perp,2})u_2 \right] \, dk'_{\perp,1} \, dk'_{\perp,2}.$$

We have used the Bragg condition to get $k_{\perp,1} = -2K(\tau(l))$; in earlier work [14], we had

$$k_{\perp,1} \cos\theta(\tau) = -2K_g(\tau). \tag{18}$$

Neglecting terms that are small in mismatch, we get

$$k_{\perp,1} \simeq -2K(\tau), \tag{19}$$

which is how the Bragg condition is typically presented in the literature: at every point along the ray, there is a specific $k_{\perp,1}$ that is responsible for backscattering, and its value is determined solely by the wavenumber at that point. Moving forward, we define the inverse of $\boldsymbol{M}_w$ as

$$\boldsymbol{M}_w^{-1} = \begin{pmatrix} M_{xx}^{-1} & M_{xy}^{-1} & 0 \\ M_{yx}^{-1} & M_{yy}^{-1} & 0 \\ 0 & 0 & 0 \end{pmatrix} = \begin{pmatrix} \begin{pmatrix} M_{xx} & M_{xy} \\ M_{yx} & M_{yy} \end{pmatrix}^{-1} & 0 \\ 0 & 0 \end{pmatrix}. \tag{20}$$

It is important to bear in mind that M_{ij}^{-1} is the ij component of $\boldsymbol{M}_w^{-1}$, and not $1/M_{ij}$.

We split the integrand in equation (15) into two parts. The first is the turbulence we are trying to measure, given by

$$\langle \delta n_e^2(t) \rangle_t \widetilde{C}_l(\omega). \tag{21}$$

The turbulence spectrum may contribute to the localisation weight. For electrostatic turbulence, references [45, 46, 47] suggest that the spectrum is of the form $\widetilde{C}(\mathbf{r}, k_{\perp,1}, k_{\mu,2}, \Delta u_\parallel, \omega) \propto k_\perp^{-10/3}$ for $k_\perp \rho_i \ll 1$ and $\widetilde{C}(\mathbf{r}, k_{\perp,1}, k_{\mu,2}, \Delta u_\parallel, \omega) \propto k_\perp^{-13/3}$ for $k_\perp \rho_i \gg 1$. Since $k_{\perp,1}$ is related to the beam's wavevector via the Bragg condition, equation (19), the turbulence spectrum localises signal to the cut-off, which we nominally take to be the point along the ray where the beam wavenumber K is at a minimum. However, we do not assume any turbulence spectrum in this paper, and neglect this

effect, maintaining generality as far as we can. The second part of equation (15) is the prefactor of the turbulence,

$$F_t = F_p \frac{g_{ant}^2}{g^2} \frac{\bar{W}_y \det\left[\mathrm{Im}\left(\boldsymbol{\Psi}_w\right)\right]}{\sqrt{2}\left|\det\left[\boldsymbol{M}_w\right]\right|\left[-\mathrm{Im}\left(M_{yy}^{-1}\right)\right]^{\frac{1}{2}}} \exp\left(-\frac{\theta_m^2}{(\Delta\theta_m)^2}\right). \tag{22}$$

This prefactor gives the localisation weight at every point along the ray; one can also think of it as a function that weighs the turbulence at various locations. Other authors have different names for analogous quantities: spatial resolution [41], instrumentation response function [48, 49], weighting function [50], or filter function [51]. We split F_t into various pieces, $F_t = F_p F_r F_b F_m$. Here we have the polarisation piece, which we referred to as ε in previous work [14],

$$F_p = \varepsilon = \frac{\Omega^4 \epsilon_0^2 m_e^2}{e^4 n_{e,\mu}^2} |\hat{\mathbf{e}}_\mu^* \cdot (\boldsymbol{\epsilon}_{eq,\mu} - \mathbf{1}) \cdot \hat{\mathbf{e}}_\mu|^2, \tag{23}$$

ray piece

$$F_r = \frac{g_{ant}^2}{g^2}, \tag{24}$$

beam piece

$$F_b = \frac{\bar{W}_y \det\left[\mathrm{Im}\left(\boldsymbol{\Psi}_w\right)\right]}{\sqrt{2}\left|\det\left[\boldsymbol{M}_w\right]\right|\left[-\mathrm{Im}\left(M_{yy}^{-1}\right)\right]^{\frac{1}{2}}}, \tag{25}$$

and mismatch piece

$$F_m = \exp\left[-2\frac{\theta_m^2(l)}{\left[\Delta\theta_m(l)\right]^2}\right], \tag{26}$$

where $\Delta\theta_m(l)$ is the characteristic width of the mismatch attenuation, given by

$$\Delta\theta_m = \frac{1}{K}\left(\frac{\mathrm{Im}\left(M_{yy}^{-1}\right)}{\left[\mathrm{Im}\left(M_{xy}^{-1}\right)\right]^2 - \mathrm{Im}\left(M_{xx}^{-1}\right)\mathrm{Im}\left(M_{yy}^{-1}\right)}\right)^{\frac{1}{2}}, \tag{27}$$

The physical intuition relating to the various contributions to $\Delta\theta_m$ is given in our earlier work [14]. To illustrate the various pieces of localisation weight, we plot them as function of arc length along the central ray in subsection 4.1.

3. Analysis of experimental data

In this section, we explain what data was studied and how we analysed it. This begins in subsection 3.1 with an introduction to the various MAST and MAST-U shots that were used for this paper. We then describe in subsection 3.2 what equilibrium data was needed. The geometry of the MAST DBS is detailed in subsection 3.3, while that of MAST-U is given in previous work [32]. Subsequently, we state and justify the initial beam parameters used for our beam tracing simulations of the MAST DBS in subsection 3.4. Finally, we detail how we analysed experimental DBS data in subsection 3.5.
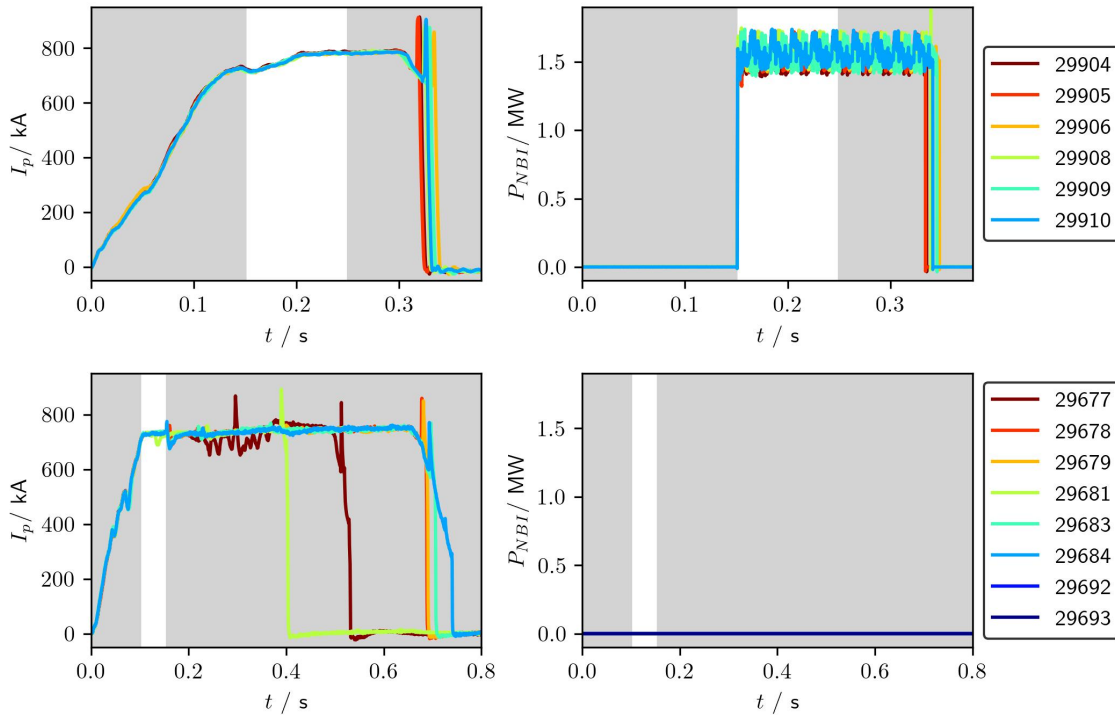
Figure 2: Shot group 1 (top) and shot group 2 (bottom). Plasma current (left) and total NBI power (right); shot group 2 was Ohmic and had no neutral beams. We studied data from the time intervals shaded in white, ignoring data from times shaded in grey. Plasma current and neutral beam power from shot group 1 was previously published [12].

3.1. Shot parameters

We study repeated shots from MAST where DBS data was available. For clarity, we split our shots into two distinct groups

> **Shot group 1** 29904, 29905, 29906, 29908, 29909, 29910
> **Shot group 2** 45288, 45289, 45290, 45291, 45292, 45293

In shot group 1, pulses were repeated with the same plasma current, shape, and heating waveforms, such that the equilibria were as similar as experimentally possible. Only the launch angle of the DBS diagnostic was varied. The shots in group 2 were also repeated shots, with significant differences only after 150 ms. The bulk of the analysis of this paper will focus on shot group 1.

In shot group 1, the MAST DBS was configured such that the V-band launched O-mode polarisation and the Q-band launched X-mode polarisation. At the point of writing, MAST-U has just started operations and only one of the two DBS systems has collected data. This system currently only has Q-band channels; further detail is available in published work [32]. In shot group 2, the Q-band launched X-mode polarised beams.
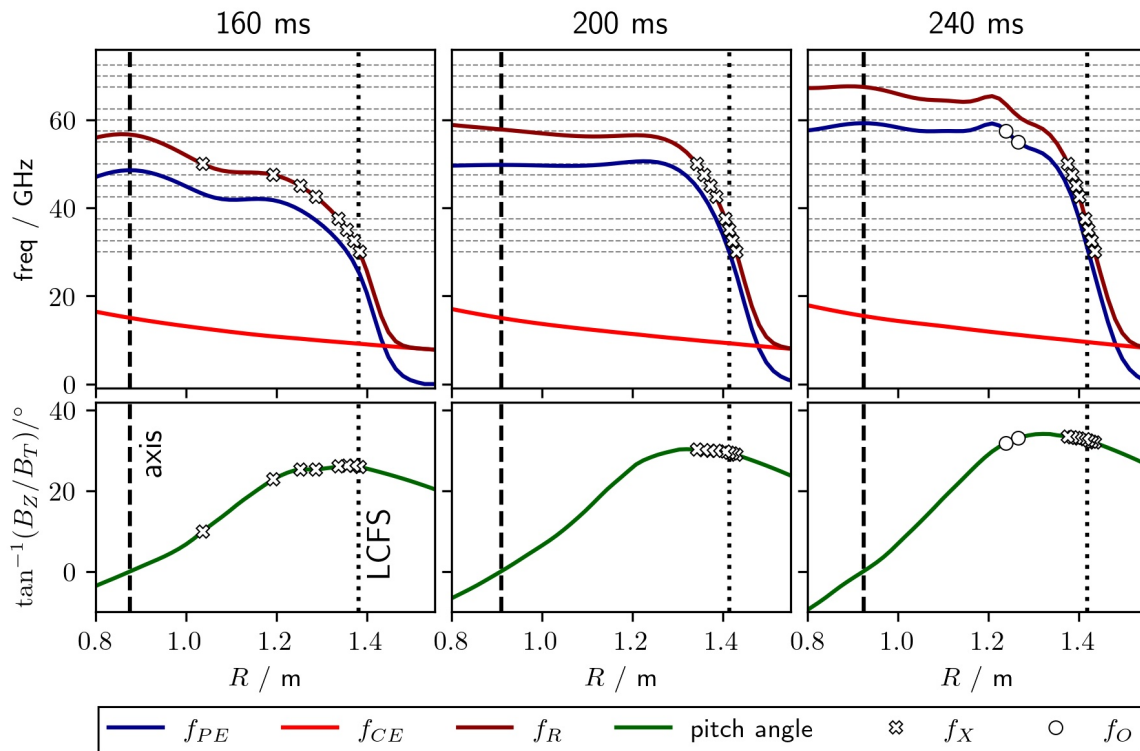
Figure 3: Properties of the plasma equilibrium for MAST shot group 1. MAST DBS frequencies indicated by the horizontal dashed lines and points (crosses for X-mode and circles for O-mode). Here f_{PE} is the plasma frequency, f_{CE} is the cyclotron frequency, f_R is the X-mode cut-off frequency, $\tan^{-1}(B_Z/B_T)$ is the pitch angle, B_Z is a poloidal component of the magnetic field, and B_T the toroidal component. These values of these quantities on the midplane are plotted as a function of radius, R.
.

3.2. Magnetic equilibria and density profiles

In order to determine the equilibrium dielectric tensor $\boldsymbol{\epsilon}_{eq}$, we need to know the electron density $n_e(\mathbf{r})$ and magnetic field $\mathbf{B}(\mathbf{r})$, both as functions of position. This is made simpler by assuming toroidal symmetry. Hence, we only need to know these quantities as expressed in the poloidal plane, as a function of R and Z. We use EFIT [52, 53], constrained by the motional Stark effect diagnostic [54] when possible, to determine the normalised poloidal flux and the toroidal magnetic field $\mathbf{B}_\zeta$. MSE-constrained EFIT was available for shot group 1 (see Table 1) but not for shot group 2. Nonetheless, since we only evaluate DBS data from scattering near the edge in shot group 2, the EFIT should be sufficiently accurate even without MSE data. The Thomson scattering diagnostic [55] gives density n_e at points along its path. Using this, together with the poloidal flux from EFIT at the points along the Thomson scattering laser beam, we express density as a function of flux label $n_e(\psi_p)$. In this work, we have used a smoothing spline for interpolation.

Shot group 1 (MAST)		
Shot number	φ_{rot}	φ_{tilt}
29904	$-4°$	$-4°$
29905	$-5°$	$-4°$
29906	$-6°$	$-4°$
29908	$-3°$	$-4°$
29909	$-2°$	$-4°$
29910	$-1°$	$-4°$

Shot group 2 (MAST-U)		
Shot number	φ_t	φ_p
45288	$2.2°$	$-2.5°$
45289	$0.9°$	$-2.5°$
45290	$3.5°$	$-2.5°$
45291	$4.6°$	$-2.5°$
45292	$4.6°$	$-2.5°$
45293	$0.1°$	$-2.5°$

Table 1: Summary of shots examined in this paper, together with the DBS mirror angles (MAST) and launch angles (MAST-U). For shot group 1, the Q-band was in X-mode and the V-band was in O-mode. Shot group 2 only had Q-band measurements in O-mode.

We use the equilibrium dielectric tensor, as determined from EFIT and Thomson scattering, as input for our beam tracing code, Scotty [14]. Scotty first determines the probe beam's electric field via beam tracing. It subsequently calculates the mismatch attenuation and other localisation weights. Such calculation only requires the beam parameters and some post-processing with our model, so one is not limited to using Scotty; any beam tracing code (such as Torbeam [44]) would suffice.

3.3. Geometry of DBS hardware

The DBS system on MAST-U is described in another paper [32]. While the MAST DBS was also covered in previous work [12], we proceed to show its setup in further detail. Detailed system geometry helps set the groundwork for a later section, where we argue that the MAST Q-band has a slight systematic error. Direct measurement of this error is no longer possible because this DBS system has already been dismantled.

The MAST DBS had two horns, one for the Q-band (30GHz–50GHz) and the other for the V-band (55GHz–75GHz). Both of these horns had their own focusing lenses shown in Figure 4. After some other optics [12], the beams were incident, at the same angle, on a steering mirror. This mirror was used to control the poloidal and toroidal launch angles of the beam. It is important to realise that the mirror angles,
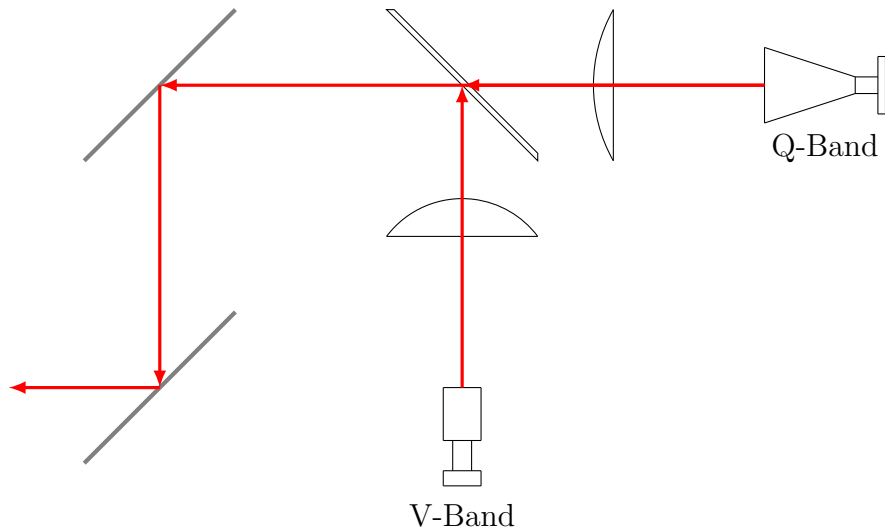
Figure 4: Simplified 2D schematic of the horns, lenses, polariser, and mirrors. The Q-band beam is transmitted through the polariser, while the V-band beam is reflected off it; this is why the polarisation of the two bands are always orthogonal to each other. The polariser is adjusted such that one band is in O-mode and the other X-mode. The last mirror here is the steering mirror, which appears in Figure 5. For a 3D view of the experimental layout, refer to Figure 6 of previous work on the MAST DBS [12].

which we call rotation φ_{rot} (left and right) and tilt φ_{tilt} (up and down), are related to the Scotty (as well as other codes, like Torbeam and Genray) launch angles by a 3D transformation. A positive φ_{tilt} corresponds to the normal of the mirror pointing towards the ceiling (and negative corresponds to pointing towards the ground). The sign convention for φ_{rot} is given in Figure 5. When $\varphi_{rot} = 0$ and $\varphi_{tilt} = 0$, the beam is incident on the mirror at 45° and reflected at 45°, subsequently propagating in the midplane of the tokamak. However, $\varphi_{rot} = 0$ does not correspond to the beam being launched in the radial direction (straight toward the centre column); in this situation, the beam does not propagate towards the centre of the central column, but is displaced to the side by 12.5cm as shown in Figure 5. Those wishing to analyse data from the old MAST DBS would do well to take meticulous care to ensure that all the above issues are properly accounted for. In the laboratory Cartesian system (X, Y, Z), the mirror normal is given by

$$\hat{\mathbf{n}}_{mirror} = \begin{pmatrix} \cos \varphi'_{rot} & -\sin \varphi'_{rot} & 0 \\ \sin \varphi'_{rot} & \cos \varphi'_{rot} & 0 \\ 0 & 0 & 1 \end{pmatrix} \left[\begin{pmatrix} 1 & 0 & 0 \\ 0 & \cos \varphi_{tilt} & -\sin \varphi_{tilt} \\ 0 & \sin \varphi_{tilt} & \cos \varphi_{tilt} \end{pmatrix} \begin{pmatrix} 0 \\ 1 \\ 0 \end{pmatrix} \right], \tag{28}$$

where we use the shorthand

$$\varphi'_{rot} = \frac{\pi}{4} + \varphi_{rot} - \arctan \frac{2155}{125}. \tag{29}$$

The arctangent accounts for an angular offset, which is illustrated in Figure 5. With the normal vector of the mirror, the direction of the probe beam as it propagates away
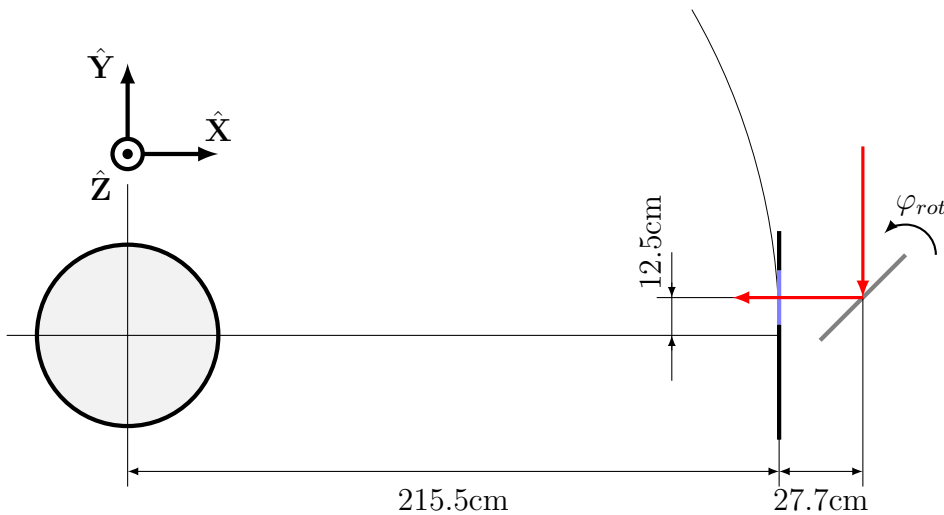
Figure 5: The steering mirror rotates around two axes, both of which pass through the point where the centre of the beam is incident on its surface. The angle φ_{rot} refers to the launch angle in the plane of the diagram, and φ_{tilt} adjusts the mirror rotation angle out of plane of the diagram. That is, they are related to the azimuthal and polar angles respectively. A positive φ_{tilt} corresponds to the normal of the mirror pointing towards the sky (and negative corresponds to pointing towards the ground). The sign convention for φ_{rot} is given in the diagram. In the diagram, we have $\varphi_{rot} = 0$ and $\varphi_{tilt} = 0$, such that the beam is incident at 45°, reflected at 45°, and propagates in the midplane of the tokamak. In this situation, however, the beam does not propagate towards the centre of the central column, but is displaced to the side by 12.5cm. The DBS was designed this way because the window was slightly offset to the side of the flange [12].

from the mirror is calculated, giving the poloidal and toroidal launch angles required as input for Scotty. The initial wavevector in the laboratory frame (R, ζ, Z) is given by

$$
\begin{aligned}
K_{R,ant} &= -\frac{\Omega}{c}\cos\varphi_t \cos\varphi_p, \\
K_{\zeta,ant} &= -\frac{\Omega}{c}R_{ant}\sin\varphi_t \cos\varphi_p, \\
K_{Z,ant} &= -\frac{\Omega}{c}\sin\varphi_p,
\end{aligned}
\tag{30}
$$

where φ_p and φ_t are the poloidal and toroidal launch angles respectively.

The hardware was such that the polarisations of the beams from the two horns of the MAST DBS were always perpendicular to each other. These polarisations were optimised such that one horn would launch an O-mode beam, and the other an X-mode beam. Here the O-mode refers to the polarisation being parallel to the magnetic field upon entering the plasma, and the X mode refers to the polarisation being perpendicular to the magnetic field upon entry.

3.4. Beam parameters

The beam parameters at launch are required as input for our beam-tracing code, Scotty. These parameters determine the initial $\boldsymbol{\Psi}_w$ at launch. In this work, we take the beam to be launched from the steering mirror's centre. The launch beam width and curvatures depend on frequency. This subsection describes and explains our choice of initial conditions.

The MAST DBS system had eight Q-band channels, as well as eight V-band channels. However, for the shots studied, the highest frequency V-band channel (75 GHz) was not digitised. The most straightforward way to determine the initial beam parameters would be to simply measure them for every channel. Since it is no longer possible to measure these parameters for the original system, we proceed with the available data. The beam width as a function of distance from the lens, for the Q-band, was measured for three different frequencies: 35 GHz, 45 GHz, and 50 GHz. For the V-band, although the beam widths were measured, these measurements were not frequency resolved. As such, we estimate the beam parameters differently for the Q and V-bands.

To get the MAST DBS Q-band parameters for all channels, we performed full-wave simulations of the horn-lens system using the commercial software CST Studios. The beam parameters are then extracted from the far field data in the E and H planes. In Appendix B, we show that there is good agreement between the simulations and measured data. In this work, we use the width and curvature in the plane parallel to the launch polarisation for simplicity. Similar techniques were used for the MAST-U DBS (Q-band only), with one difference. Instead of performing full-wave simulations of the horn, we calculate the launch beam properties from the horn's specifications. As for the MAST DBS V-band, we do not know enough about the horn to perform such simulations. Consequently, for every V-band frequency, we fit the Gaussian beam evolution to the measured far-field data as shown in Appendix B. We summarise the beam parameters at launch in Figure 6.

3.5. Spectral analysis of DBS signal

We use Welch's method of averaged periodograms [56] to calculate the spectral density, weighted with Hann windows [57] and using a 50% overlap. This method involves dividing a time period into equal segments, applying a Hann window to each of them, individually Fourier transforming them, and then finding the mean spectral density at every given frequency. The standard deviation is then used to estimate the associated standard error of the mean, which we use for error bars. In this work, we average over 101 segments. Each segment spans 0.1024ms, which gives us a total of 5.2ms, since any two adjacent segments overlap. We then smooth the spectrum. The smoothing process works as follows. We consider a moving window of 5 points, discard the highest and lowest points, and then take the mean of the remaining 3 points. This is essentially a moving trimmed average.
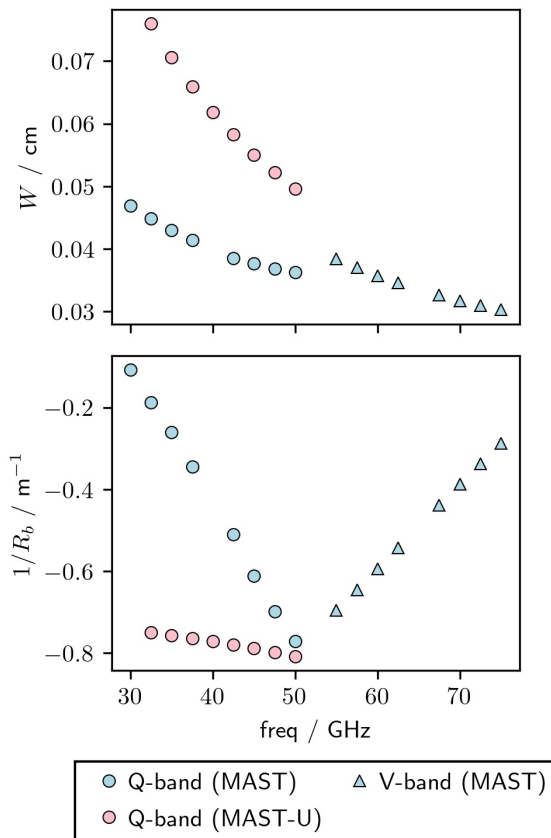
Figure 6: Beam width, W, and curvature, $1/R_b$, used as initial conditions for beam tracing for the DBS systems, as a function of frequency. The MAST Q-band's initial beam was not circular, with slightly different widths and curvatures parallel and perpendicular to the polarisation. In this work, we use the width and curvature in the plane parallel to the launch polarisation. Determination of these parameters is discussed in Appendix B.

DBS spectra are typically formed of two peaks: one centred at zero frequency, with the other at some Doppler-shifted frequency, as shown in Figure 7. The latter is believed to contain the useful backscattered signal, while the former is thought to be a spurious contribution [58]. Hence, one tries to remove the zero-frequency peak, and analyse the Doppler-shifted peak. This is typically done by fitting peaks to the spectrum, enabling one to find the Doppler shift and backscattered power of the signal. The Doppler shift is generally of interest as it sheds light on the velocity profile of the plasma. However, in this study, we are not interested in the frequency of this shift, and fitting the data is difficult because the MAST DBS Doppler-shifted peak is often asymmetric and broad; instead, we focus on the backscattered power. Consequently, the analysis procedure may be significantly simplified compared to that of previous work [12]. We find the total backscattered power at both positive and negative frequencies, and subtract the latter from the former, getting what we call the antisymmetric backscattered power (see
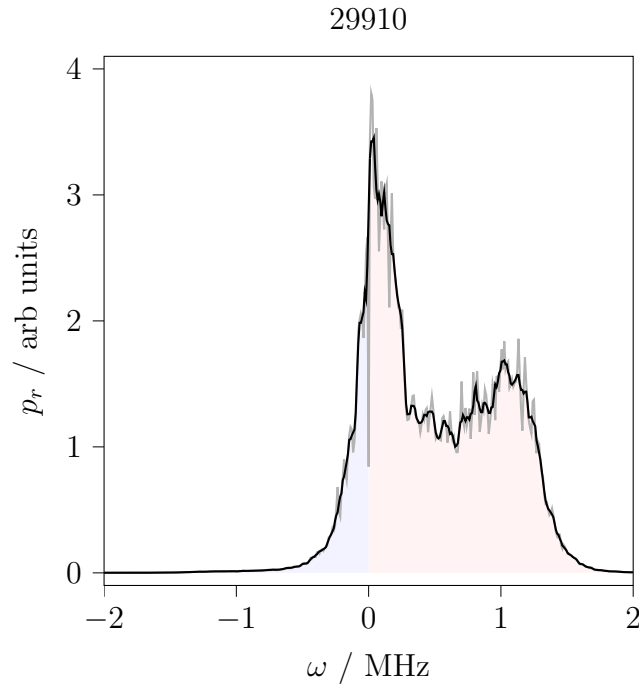
Figure 7: Welch periodogram (grey line) of the spectral density and the smoothed spectrum (black line). We calculate the backscattered power by subtracting the blue area from the red area.

Figure 7). Using the antisymmetric backscattered power for DBS analysis is a technique also used by other groups [59]. Different techniques for finding the backscattered power were also explored; they turned out to be as robust for the purposes of this work. Hence, we chose the simplest method, the one described above. As for the MAST-U DBS, we fitted the Doppler shifted peak and calculated the power accordingly.

4. Mismatch attenuations

We first describe how we use the mismatch piece and the other localisation weights to evaluate the variation of backscattered power with toroidal launch angle, subsection 4.1. We present comparison with MAST V-band data in subsection 4.3 and with MAST Q-band data in subsection 4.3.

4.1. Method of evaluating contributions to the backscattered signal

We describe how we bring together the beam model's insight on localisation weighting and experiments to calculate the effect of mismatch attenuation.

To illustrate the localisation weighting, we consider the equilibrium at 160 ms of MAST shot 29908; the details of this equilibrium were given earlier, in Section 3.2. We launch two beams, as shown in Figure 8, and calculate the various localisation weight pieces along their trajectories, shown in Figure 9. The lower frequency beam refracts

strongly and we find that the region of dominant backscattering is close to the cut-off; this is the regime where DBS is typically operated. The beam model is also applicable more broadly; the higher frequency beam transmits through the plasma with minimal refraction. In this case, we find that the region where most of the backscattering occurs is some distance from the nominal cut-off. In this paper, we will limit discussion to the former case, exploring the latter in future work.

Experimental investigation of the mismatch attenuation piece, F_m, is usually done as follows [12, 14, 16, 13, 15]. The poloidal launch angle is fixed and the toroidal launch angle varied with each repeated shot, Figure 10. We expect significant variation in only the mismatch angle. As such, the difference in backscattered powers for any given channel is attributed entirely to the mismatch attenuation. We find that there is indeed a small variation in the cut-off location and the corresponding wavenumber at that location as the toroidal launch angle is varied. This is illustrated in Figure 11. We now plot the various localisation weights, finding that they do indeed affect both the width and the peak of how one expects the backscattered power to vary with toroidal launch angle and thus mirror rotation angle, Figure 12. Comparing the beam model's prediction with preliminary data from MAST-U, we find that the total localisation is better at predicting the variation of backscattered power with toroidal launch angle than the mismatch piece alone, Figure 13.

In the next section, we extend our analysis by studying all channels of the MAST Q and V bands at various times.

4.2. Comparison with data: V-band

We limit ourselves to cases where most of the backscattered signal comes from the region around the cut-off, as shown in Figure 8. This corresponds to the lower frequency channels at later times in the shots, when the electron densities were higher.

We find that the mismatch attenuation and total localisation weight pieces, both evaluated at the cut-off, predict similar variations of backscattered power as a function of φ_{rot}. To summarise large amounts of data, we compare the $1/e^2$ halfwidths instead of the full functions in Figure 13. These results are shown in Figure 14. The beam model's predictions largely agree with experiments; the experimental fit's error bars are large because the toroidal sweep was coarse, with only three of the six repeated shots having significant backscattered power. This is the first systematic analysis which shows that the beam model of DBS accounts for the backscattered O-mode signal. Previous work either focused exclusively on X-mode [16, 15] or only a single channel at a single time [14]. Interestingly, we see that the mismatch tolerance, $\Delta\theta_{m,c}$, does not change significantly with time. Here the subscript $_c$ indicates evaluation of the quantity at the nominal cut-off location, that is, the point along the central ray where the beam's wavenumber is minimised.
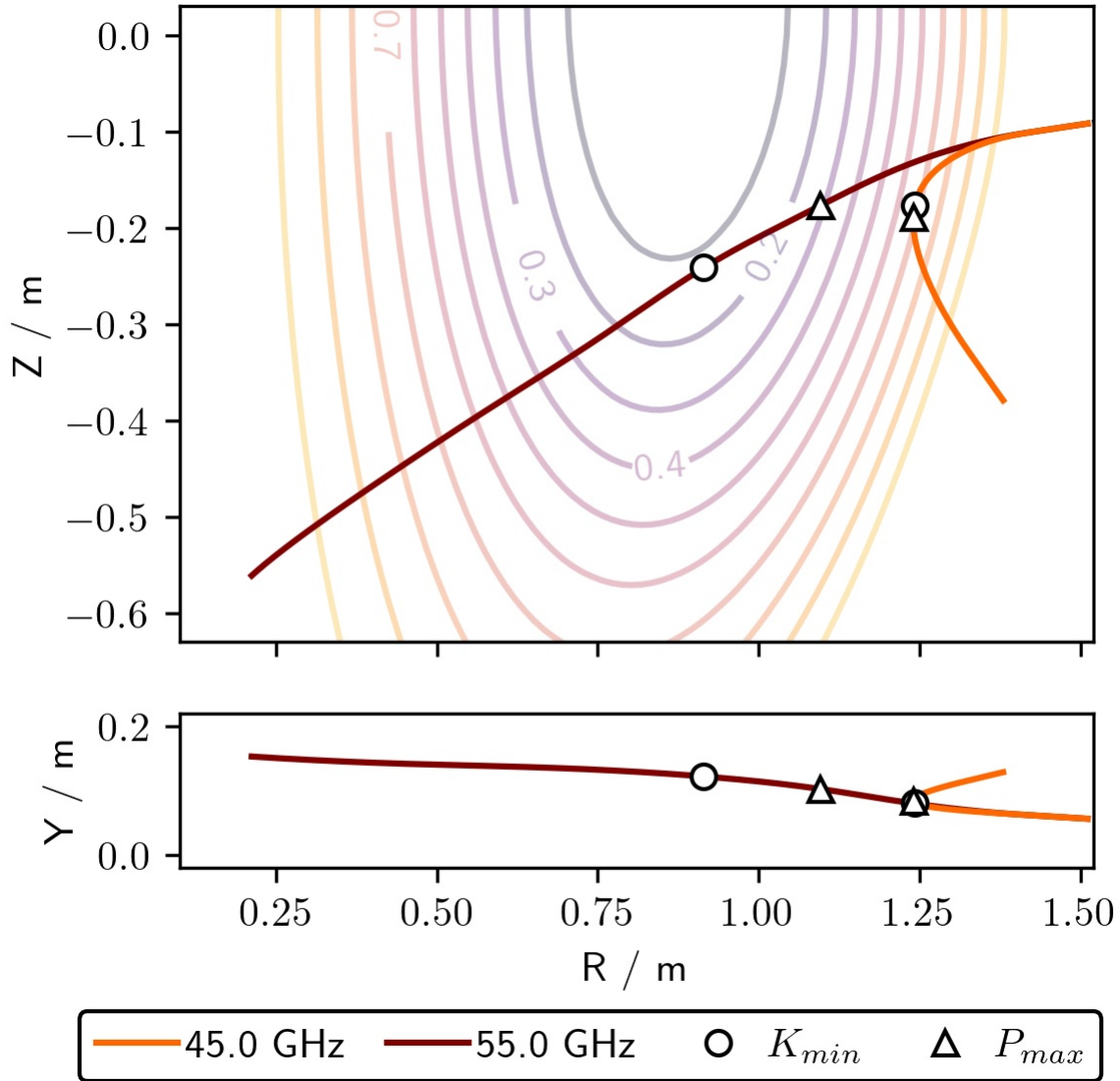
Figure 8: Paths of the 30 GHz (orange) X-mode and 55.0 GHz (red) O-mode probe beams at 160 ms. These beams have the same poloidal and toroidal launch angles. The circles mark the nominal cut-off locations, where the beams' wavecnumbers are minimised. The triangles mark the locations of maximum scattering, as calculated from the localisation weighting, shown in Figure 9. In these paper, we limit our analysis to cases where the location of maximum scattering is close to the cut-off location; that is, cases like those denoted by the orange line but not the red line.
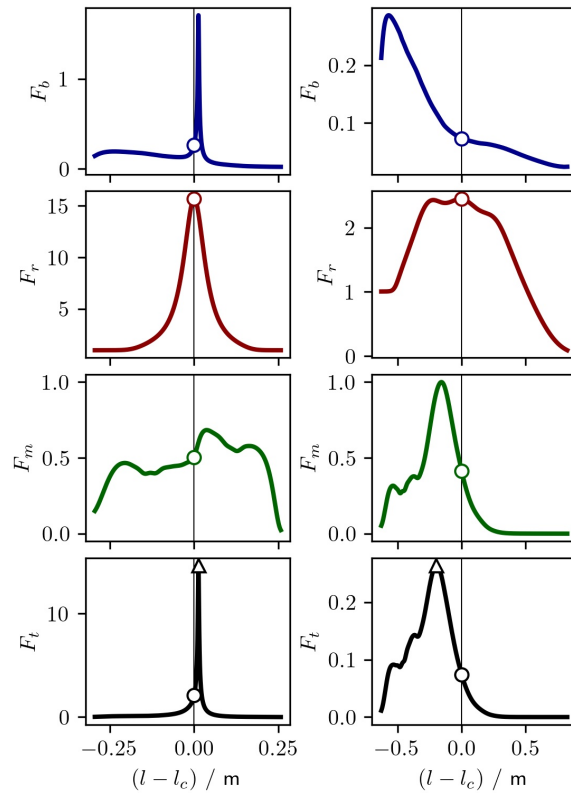
Figure 9: Localisation of the 45 GHz (left) and 55.0 GHz (right) probe beams at 210ms and $\varphi_{rot} = -0.4°$ as a function of arc length along the ray from the nominal cut-off location. In cases exemplified by the plot on the left, the backscattered signal mostly comes from the cut-off region. In other cases, the large mismatch at the cut-off causes the dominant backscattering location to be shifted to a region where there is less mismatch attenuation. For the MAST DBS, the diverging beam results in the beam localisation-weight piece decreasing as the beam propagates. Hence, for longer paths, this piece also reduces the signal coming from the cut-off location. All pieces of the localisation weight have been normalised to their respective values at the point of entry into the plasma.

4.3. Comparison with data: Q-band

Analysis of the Q-band data is more challenging. As we see from Figure 15, there is a systematic discrepancy between the experimental data and our model. We assume that there is some misalignment in the Q-band optics that is equivalent to a systematic 3.0° error in the mirror angle. This mostly accounts for the aforementioned discrepancy.

Since the lens had quite a short focal length, a slight ~ 1 mm transverse offset of the lens relative to the horn would already steer the beam enough to account for the 3.0° error. Alternatively, the Q-band horn may simply not have been angled correctly. Analysis of other repeated shots on MAST indicate a similarly-sized error, but the results are not as conclusive as that from shot group 1. We find that this error changes slightly, less than a degree, at different times in shot group 1. Unfortunately, the MAST DBS
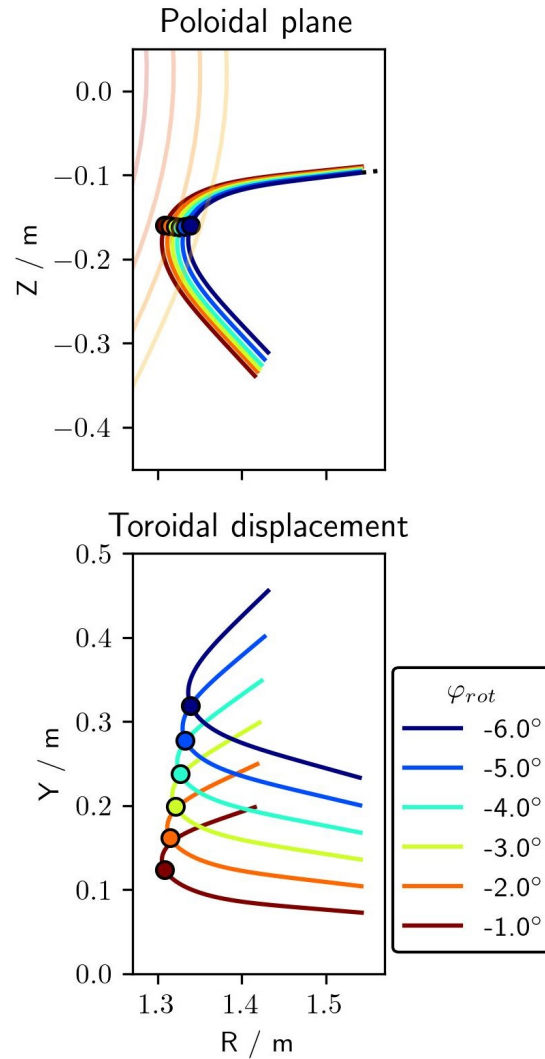
Figure 10: We show the trajectories of the 55GHz MAST DBS probe beam at 240ms. These beams are launched with different toroidal angles, corresponding to the angles in shot group 1, and reach the cut-off at similar flux surfaces. For each ray, the circle marks the cut-off location, defined to be the point where the wavenumber K is minimised.

was removed immediately after MAST's final campaign; calibration and more detailed measurements are no longer possible.

Assuming a fixed systematic error of 3° for all Q-band channels at all times, we find that there is good agreement between the beam model and experimental data, Figure 16.
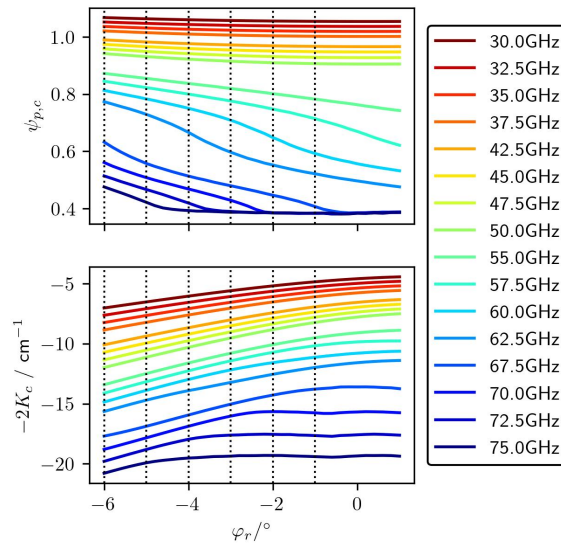
Figure 11: The normalised flux surface label (top) and backscattered wavenumber (bottom) at the cut-off for different frequencies and launch angles, for MAST shot group 1 at 240 ms. The 55GHz line summarises Figure 10. The experimental mirror rotation angles are given by the vertical dotted lines; they run from $-6°$ to $-1°$, as shown in Table 1.

5. Conclusion

In this work, we extend previous analysis of mismatch [12, 16, 15] to more times and frequencies on MAST and MAST-U, showing that mismatch attenuation of the backscattered signal is indeed of general importance. We proceed to demonstrate that the beam model of DBS [14] is able to quantitatively determine the mismatch attenuation, which is crucial for interpreting the DBS signal. This paves the way for reliable and quantitative accounting of mismatch attenuation in all future DBS studies, which has two advantages: better interpretation of DBS data and loosening of the requirement that the beam wavevector has to be exactly perpendicular to the magnetic field at the cut-off. As long as the mismatch angle is not so large that the signal is below the noise floor, the beam model allows one to correct for this effect and use the backscattered signal for other studies.

The strong dependence of the backscattered signal on mismatch angle raises the possibility of using DBS as a method of measuring magnetic pitch angle in the core, an attractive prospect since DBS is likely able to survive the harsh environment of burning plasmas. If a high level of precision is required for the pitch angle, we show it is important to account for the additional localisation weights, in addition to the mismatch attenuation.

Returning to the bigger picture, we have demonstrated that the beam model of DBS is applicable to real plasmas. Using beam tracing, which is only marginally more complicated than ray tracing, together with our analysis techniques, enables deeper
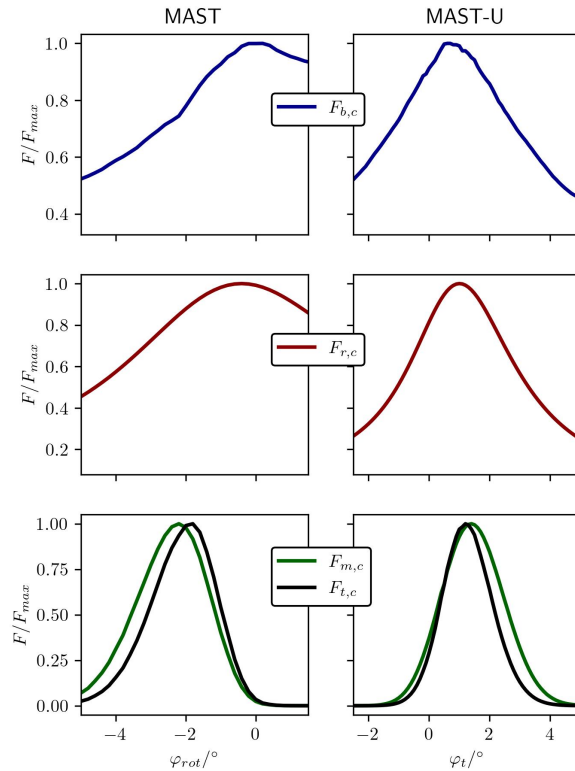
Figure 12: Localisation weights at the cut-off as a function of mirror rotation angle (MAST) and toroidal launch angle (MAST-U); 32.5 GHz X-mode for both systems. Here the subscript $_c$ indicates evaluation of the quantity at the nominal cut-off location, that is, the point along the central ray where the beam's wavenumber is minimised. This figure summarises the circles in Figure 9 for multiple launch angles but different frequencies. We see that the change in backscattered power is mostly due to the mismatch attenuation; the other pieces have a small effect on both the width and peak of this variation (bottom subplots).
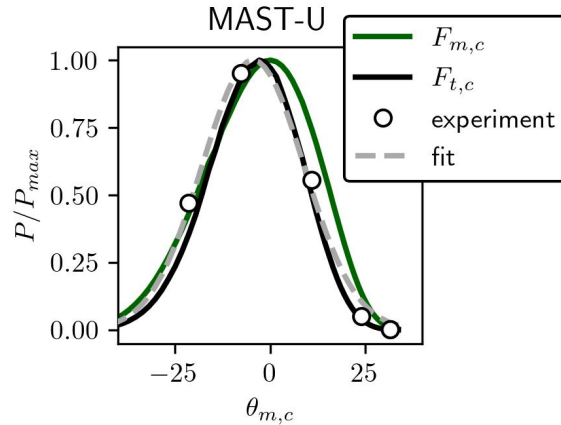
insight to be gained.

Acknowledgments

Figure 13: Comparison of experimental data (points) and Gaussian fit of experimental data (dashed gray line) with the beam model's predictions: mismatch attenuation alone (solid green line) and the product of mismatch attenuation with the other localisation weights (solid black line). The subscript $_c$ indicates evaluation at the nominal cut-off location, that is, the point along the ray where the wavenumber is minimised. Note that while $F_{m,c}$ is a Gaussian function of θ_m, this is generally not the case for F_t , hence we do not expect experimental data to be a Gaussian either; the fit is merely to give indicative results.
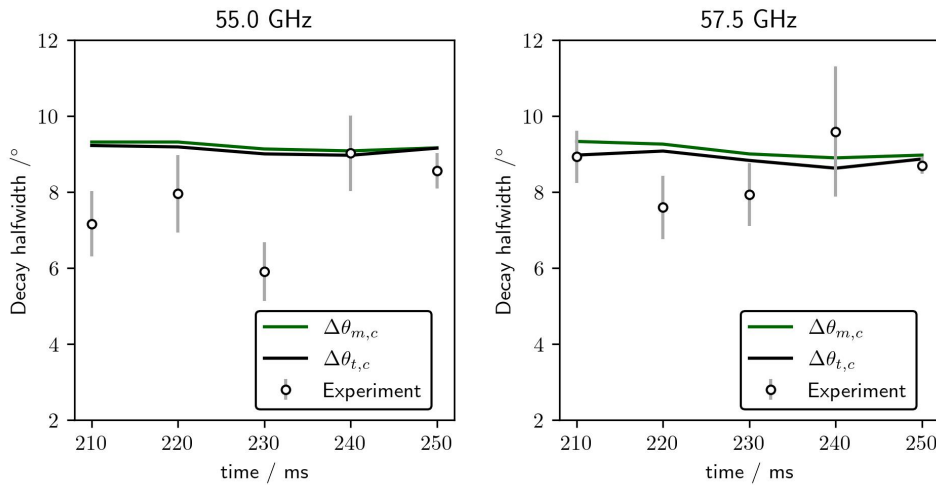

Figure 14: The decay halfwidths of backscattered power as a function of mismatch angle, θ_m, for shot group 1: Gaussian fits of experimental data (points), the mismatch tolerance piece (green line), and the total localisation piece (black line). These were O-mode channels. In this situation, we see that the other localisation weights do not have a significant effect on the mismatch tolerance.
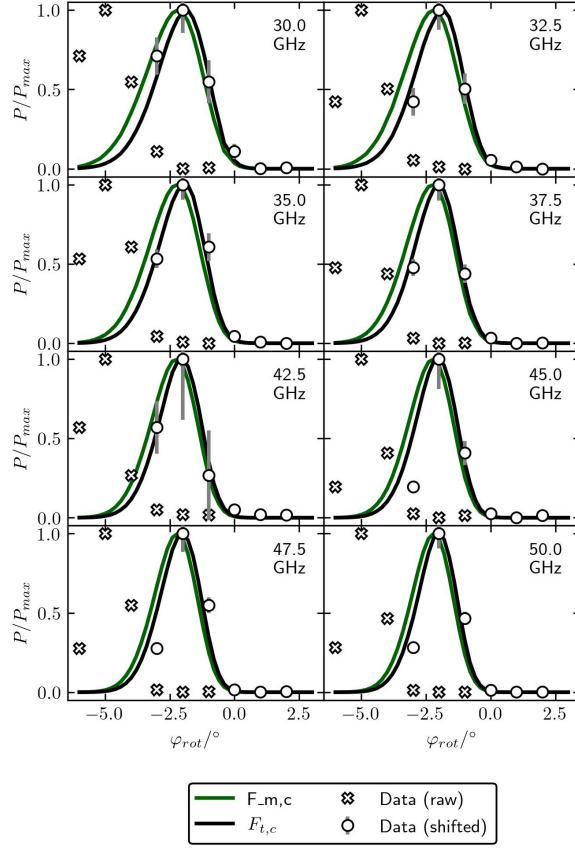
Figure 15: Q-band data from shot group 1 at 200ms. Data (crosses), data assuming that there was a slight error in the launch angle (circles), model of the mismatch-attenuated backscattered signal from the cut-off (black line), model of backscattered signal (solid black line).

Appendix A. M_w: the effective Ψ_w

The matrix $\boldsymbol{M}_w$ is given by

$$\boldsymbol{M}_w = \begin{pmatrix} M_{xx} & M_{xy} & 0 \\ M_{xy} & M_{yy} & 0 \\ 0 & 0 & 0 \end{pmatrix}, \tag{A.1}$$

where

$$M_{xx} = \Psi_{xx} - \frac{K_g}{\cos\theta}\left(\frac{\sin\theta}{g}\frac{d\theta}{d\tau} - \boldsymbol{\kappa}\cdot\hat{\mathbf{x}}\sin\theta + \hat{\mathbf{x}}\cdot\nabla\hat{\mathbf{b}}\cdot\hat{\mathbf{g}} - \hat{\mathbf{x}}\cdot\nabla\hat{\mathbf{b}}\cdot\hat{\mathbf{x}}\tan\theta\right), \tag{A.2}$$

$$M_{xy} = \Psi_{xy} - \frac{K_g}{\cos\theta}\left(-\boldsymbol{\kappa}\cdot\hat{\mathbf{y}}\sin\theta + \hat{\mathbf{y}}\cdot\nabla\hat{\mathbf{b}}\cdot\hat{\mathbf{g}} + \frac{\sin\theta\tan\theta}{g}\frac{d\hat{\mathbf{x}}}{d\tau}\cdot\hat{\mathbf{y}} - \hat{\mathbf{y}}\cdot\nabla\hat{\mathbf{b}}\cdot\hat{\mathbf{x}}\tan\theta\right), \tag{A.3}$$

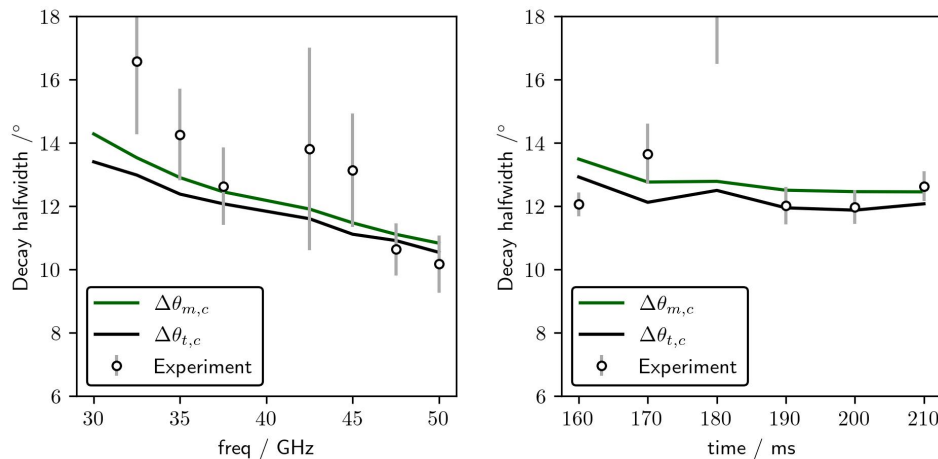and

$$M_{yy} = \Psi_{yy}. \tag{A.4}$$

Figure 16: The decay halfwidths of backscattered power as a function of mismatch angle, θ_m, for shot group 1: Gaussian fits of experimental data (points), the mismatch tolerance piece (green line), and the total localisation piece (black line). These were X-mode channels. All channels at 210ms (left) and various times for the 37.5GHz channel (right).

Here the subscripts give the relevant directions of $\boldsymbol{M}_w$, shown in Figure 1; the angle

$$\cos\theta = \hat{\mathbf{g}} \cdot \hat{\mathbf{u}}_1 \tag{A.5}$$

is related to the angle between the group velocity and magnetic field, also shown in Figure 1, and

$$\boldsymbol{\kappa} = \frac{1}{g}\frac{\mathrm{d}\hat{\mathbf{g}}}{\mathrm{d}\tau} \tag{A.6}$$

is the curvature of the central ray. This ray curvature should not be confused with the wavefront curvature, R_b. In general, the real and imaginary parts of $\boldsymbol{M}_w$ are not simultaneously diagonalisable, as was the case for $\boldsymbol{\Psi}_w$. In this formulation of $\boldsymbol{M}_w$, we have used the Bragg condition to evaluate $k_{\perp,1}$ along the ray, and $k_{\perp,2} = 0$; the argument for this was presented in our previous work [14]. To simplify $\boldsymbol{M}_w$, we neglect terms that are small in mismatch angle [14], getting

$$M_{xx} \simeq \Psi_{xx} - K\left(\hat{\mathbf{b}} \cdot \nabla\hat{\mathbf{b}} \cdot \hat{\mathbf{g}}\right), \tag{A.7}$$

$$M_{xy} \simeq \Psi_{xy} - K\frac{\left[\left(\hat{\mathbf{b}} \times \hat{\mathbf{g}}\right) \cdot \nabla\hat{\mathbf{b}} \cdot \hat{\mathbf{g}}\right]}{\left|\hat{\mathbf{b}} \times \hat{\mathbf{g}}\right|}, \tag{A.8}$$

and

$$M_{yy} = \Psi_{yy}. \tag{A.9}$$

Note that the corrections are related to the curvature of field lines and magnetic shear, not the curvature of the cut-off.
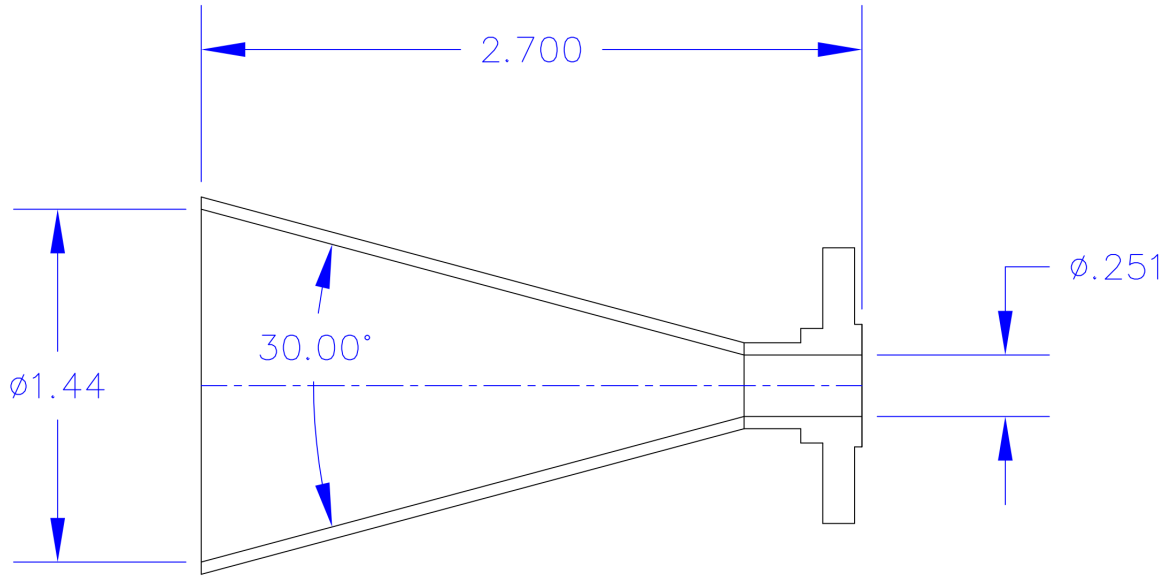
Figure B1: Lengths given in inches.

Appendix B. MAST DBS beam parameters

In this appendix, we present the methods and data used to determine the MAST DBS initial conditions required by our beam-tracing code, Scotty. At the point of writing, the MAST DBS had long since lost its original configuration. Hence, a straightforward measurement of beam properties is not possible. As such, we have seek to figure out what the launch beam widths and curvatures are, given the data we have and what we know of the horn-lens system. In the Q-band, we have three frequency resolved measurements. For each frequency, the beam widths were measured at various distances from the flat of the lens. In the V-band, similar measurements were done, but they were not frequency resolved; the measured beam width had all frequencies contributing to it at once.

A detailed description of the DBS setup is given in previous work [12]. For each of both bands, there was a horn antenna and a lens in front of it. The Q-band antenna was a standard smooth brass conical horn (Figure B1). On the other hand, the V-band antenna was a custom-made narrow-beam corrugated scalar horn, model: Quinstar QSH-V2500. Its frequency band followed the WR-15 standard (50–75GHz), the far-field full width at half maximum was 25° in the mid-band (62.5GHz), and it was fed with a circular waveguide with a diameter of 0.165 inches. Quinstar's catalogue claims that the emission pattern is highly symmetric, and thus the far-field beam properties do not depend on the plane of measurement.

As for the lenses, they were aspherical hyperbolic-planar. As the name implies, one side of the lens is planar, and the other is hyperbolic. The lenses were designed such that rays originating from the focal point would leave the lens parallel to the optic axis (Figure B2). We do not further discuss the design considerations in this paper. We use

Lens parameter	Q-band	V-band
R_l/cm	-15.5	-8.78
k	-0.594	-0.588
D/cm	20	19.5
F/cm	27	12.5

Table B1: Parameters for describing the hyperbolic side of the lens. Here R_l is the radius of curvature of the lens in question, k its conic constant, D the diameter, and F the focal length. We take the refractive indices for both lenses to be $N = 1.53$.
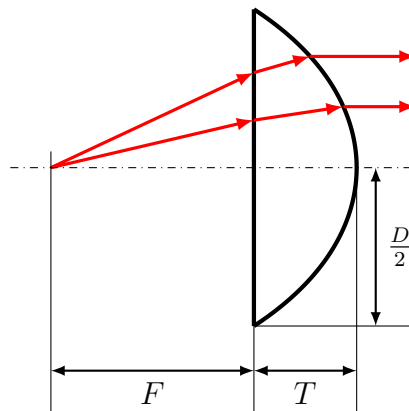

Figure B2: Both lenses are made of high-density polyethylene which has a refractive index of $N = 1.53$. The Q-band lens has focal length $F = 27\text{cm}$ and diameter $D = 20\text{cm}$, while the V-band lens $F = 12.5\text{cm}$ and diameter $D = 19.5\text{cm}$. The locus of points on the curved side (X, Y) is given by equation (B.1). The flat side of the Q-band lens was 27cm away from the aperture of the corresponding horn, while this distance was 13.9cm for the V-band horn.

a fit to describe the hyperbolic side of the lens,

$$X = \frac{Y^2 R_l^{-1}}{1 + \left[1 - (1 + k) Y^2 R_l^{-2}\right]^{1/2}}. \tag{B.1}$$

Here X and Y are the horizontal and vertical coordinates of the hyperbolic surface, R_l is the radius of curvature of the lens, and k is the conic constant. The fit parameters and lens diameter and focal lengths are given in Table B1 and illustrated in Figure B2. We take the refractive indices for both lenses to be $N = 1.53$. The notation used in this appendix is separate from the rest of the paper.

Using this information, we run full-wave simulations of the horn-lens system to determine the Q-band beam properties. To reduce simulation time, we split this into two steps. First, the emission pattern of the Q-band antenna is simulated in CST Microwave Studio. Secondly, we feed the results into a larger simulation area, which includes the lens, as shown in Figure B3 (top). We fit a Gaussian function to the beam
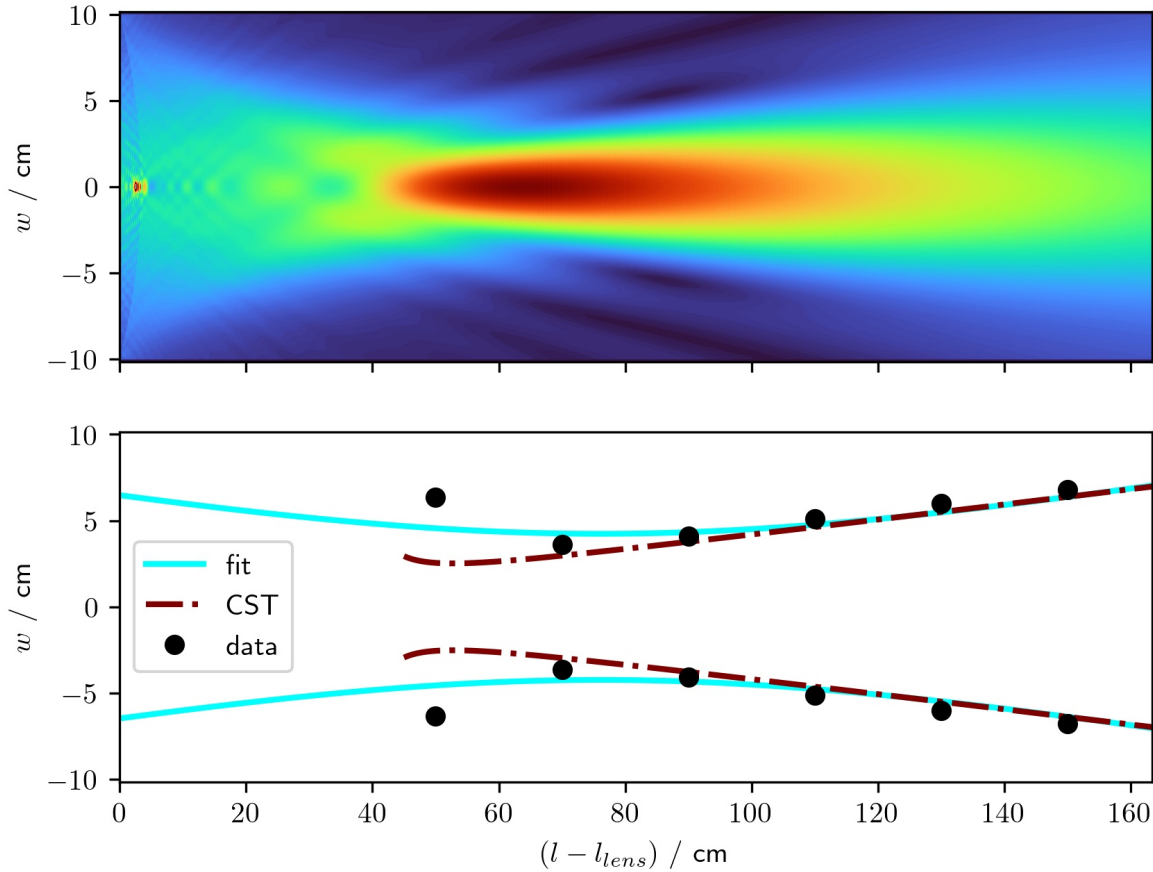
Figure B3: Magnitude of the electric field (top) and the extracted beam properties (bottom) for 35GHz.

profile, and extract the associated width. Interestingly, the beam does not reach the far field, and the profile is significantly non-Gaussian (in both simulations and in the data collected), until at least 50cm from the lens. As such, we fit a Gaussian beam to these widths only at distances which we are confident are in the far-field Figure B3 (bottom). We only fit the central lobe, as the side lobes in these simulations are larger than that measured. We find that our simulations do indeed match the data well, and so we use our simulations to determine the beam properties for the Q-band antenna.

The design of V-band horn was more complex, and we do not have enough of its details to be able to run a meaningful simulation. Hence, our approach to finding its beam widths is less sophisticated than that of the Q-band. We fit all frequencies in the V-band to the far field data as shown in Figure B4.

We explored using horn properties, together with the thin lens approximation, to find the initial beam conditions. The result was in the right ballpark. However, as seen from Figure B2, the lenses were thick and aspherical. Hence, we calculated the appropriate ray transfer matrices for the hyperbolic lenses. We ray-traced paraxial rays through the lenses in Zemax OpticStudio 21.2. For a given lens, two paraxial rays were
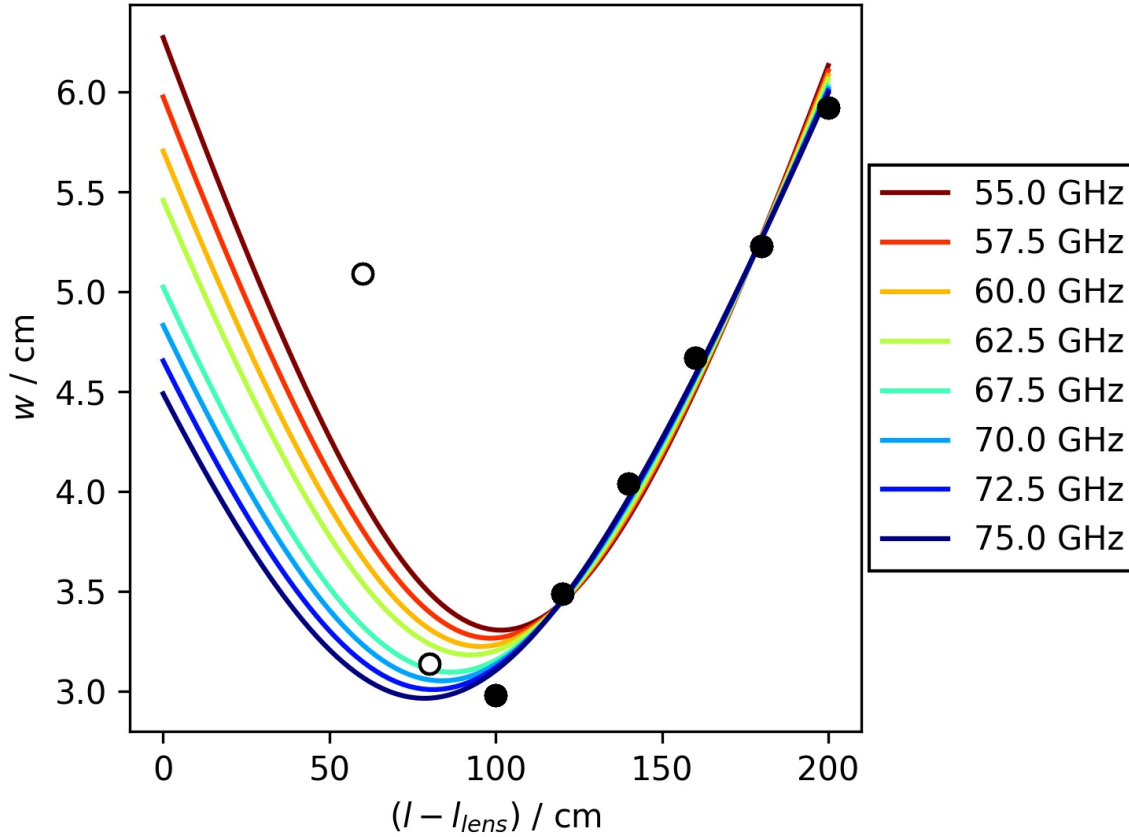
Figure B4: We use the far-field data (black-filled points) to get the beam properties for the V-band frequencies.

launched, both incident on the planar side: the first on the optical axis with a small angle of incidence, the second a small distance from the optical axis and at normal incidence. The positions and directions of both rays at the output plane were then used to calculate the ray transfer matrix. We compared the measured Q-band beam properties with that calculated from the initial beam conditions and the ray transfer matrix, and the agreement between the calculated and measured widths and curvatures was good. We tried repeating this for the V-band, but did not manage to get decent results, likely because the initial conditions at the horn were not well-specified. Particularly, while we were able to calculate the width of the beam waist from the far-field full with at half maximum, we do not know where the waist actually is. We took it to be at the mouth of the horn, but this assumption is likely to be poor, given the poor results.

References

[1] Hillesheim J, Parra F, Barnes M, Crocker N, Meyer H, Peebles W, Scannell R and Thornton a 2015 *Nuclear Fusion* **55** 032003 ISSN 0029-5515 (*Preprint* 1407.2121v2) URL http://stacks.iop.org/0029-5515/55/i=3/a=032003?key=crossref.5d8898a9db7caab7b45d6b63e116d164

[2] Conway G D, Scott B, Schirmer J, Reich M, Kendl A and Team t A U 2005 *Plasma Physics and Controlled Fusion* **47** 1165–1185 ISSN 0741-3335

[3] Conway G D, Poli E, Happel T *et al.* 2010 *Plasma and Fusion Research* **5** S2005–S2005

[4] Schmitz L 2017 *Nuclear Fusion* **57** 025003

[5] Tynan G, Fujisawa A and McKee G 2009 *Plasma Physics and Controlled Fusion* **51** 113001

[6] Pratt Q, Rhodes T L, Chrystal C and Carter T A 2022 *Plasma Physics and Controlled Fusion*

[7] Hirsch M, Holzhauer E, Baldzuhn J, Kurzan B and Scott B 2001 *Plasma Physics and Controlled Fusion* **43** 1641–1660 ISSN 07413335

[8] Hillesheim J C, Peebles W A, Rhodes T L, Schmitz L, Carter T A, Gourdain P A and Wang G 2009 *Review of Scientific Instruments* **80** ISSN 00346748

[9] Volpe F A 2017 *Journal of Instrumentation* **12** C01094

[10] Costley A E 2010 *IEEE Transactions on Plasma Science* **38** 2934–2943

[11] Rhodes T, Peebles W, Nguyen X, VanZeeland M, Degrassie J, Doyle E, Wang G and Zeng L 2006 *Review of scientific instruments* **77** 10E922

[12] Hillesheim J, Crocker N, Peebles W, Meyer H, Meakins A, Field A, Dunai D, Carr M, Hawkes N, Team M *et al.* 2015 *Nuclear Fusion* **55** 073024

[13] Damba J, Hong R, Pratt Q and Rhodes T 2021 *Bulletin of the American Physical Society*

[14] Hall-Chen V H, Parra F I and Hillesheim J C 2022 *Plasma Physics and Controlled Fusion* **64** 095002

[15] Damba J, Pratt Q, Hall-Chen V H, Hong R, Lantsov R, Ellis R and Rhodes T 2022 *Review of Scientific Instruments* **93** 103549

[16] Hall-Chen V H, Damba J, Parra F I, Pratt Q T, Michael C A, Peng S, Rhodes T L, Crocker N A, Hillesheim J C, Hong R *et al.* 2022 *Review of Scientific Instruments* **93** 103536

[17] Hong R, Rhodes T, Wang G and Peebles W 2021 *Review of Scientific Instruments* **92** 063505

[18] Mazzucato E 2006 *Plasma physics and controlled fusion* **48** 1749

[19] Hennequin P, Honoré C, Truc A, Quéméneur A, Lemoine N, Chareau J M and Sabot R 2004 *Review of Scientific Instruments* **75** 3881–3883

[20] Happel T, Estrada T, Blanco E, Tribaldos V, Cappa A and Bustos A 2009 *Review of Scientific Instruments* **80** 073502

[21] Zhou C, Liu A, Zhang X, Hu J, Wang M, Li H, Lan T, Xie J, Sun X, Ding W *et al.* 2013 *Review of Scientific Instruments* **84** 103511

[22] Happel T, Görler T, Hennequin P, Lechte C, Bernert M, Conway G, Freethy S, Honoré C, Pinzón J, Stroth U *et al.* 2017 *Plasma Physics and Controlled Fusion* **59** 054009

[23] Shi Z, Zhong W, Jiang M, Yang Z, Zhang B, Shi P, Chen W, Wen J, Chen C, Fu B *et al.* 2016 *Review of Scientific Instruments* **87** 113501

[24] Rhodes T L, Barada K, Peebles W A and Crocker N A 2016 *Review of Scientific Instruments* **87** 11E726

[25] Hu J, Zhou C, Liu A, Wang M, Doyle E, Peebles W, Wang G, Zhang X, Zhang J, Feng X *et al.* 2017 *Review of Scientific Instruments* **88** 073504

[26] Tokuzawa T, Tsuchiya H, Tsujimura T, Emoto M, Nakanishi H, Inagaki S, Ida K, Yamada H, Ejiri A, Watanabe K Y *et al.* 2018 *Review of Scientific Instruments* **89** 10H118

[27] Molina Cabrera P, Coda S, Porte L, Smolders A and Team T 2019 *Review of Scientific Instruments* **90** 123501

[28] Wen J, Shi Z, Zhong W, Yang Z, Yang Z, Wang B, Jiang M, Shi P, Hillesheim J, Freethy S *et al.* 2021 *Review of Scientific Instruments* **92** 063513

[29] Tokuzawa T, Tanaka K, Tsujimura T, Kubo S, Emoto M, Inagaki S, Ida K, Yoshinuma M, Watanabe K, Tsuchiya H *et al.* 2021 *Review of Scientific Instruments* **92** 043536

[30] Carralero D, Happel T, Estrada T, Tokuzawa T, Martínez J, de la Luna E, Cappa A and García J 2021 *Fusion Engineering and Design* **173** 112803

[31] Yashin A, Bulanin V, Petrov A and Ponomarenko A 2021 *Applied Sciences* **11** 8975

[32] Rhodes T L, Michael C A, Shi P, Scannell R, Storment S, Pratt Q, Lantsov R, Fitzgerald I,

Hall-Chen V H, Crocker N A and Peebles W A 2022 *Review of Scientific Instruments* **93** 000000

[33] Harrison J R 2021 Overview of first results from mast upgrade *28th IAEA Fusion Energy Conference* https://conferences.iaea.org/event/214/contributions/18686/

[34] Gerhardt S 2021 NSTX-U recovery project progress towards first plasma *28th IAEA Fusion Energy Conference* https://conferences.iaea.org/event/214/contributions/17249/

[35] Department for Business, Energy and Industrial Strategy 2021 Towards fusion energy: the uk fusion strategy *Policy paper* https://www.gov.uk/government/publications/towards-fusion-energy-the-uk-fusion-strategy

[36] Shi Z B, Wen J, Wang B, Yang Z C, Zhong W L, Hillesheim J C, Freethy S, Jiang M, Shi P W, Fang K R, Liu Z T and Xu M 2019 *Proceedings of the 14th International Reflectometry Workshop for Fusion Plasma Diagnostics* URL https://www.aug.ipp.mpg.de/IRW/IRW14/proceedings.html

[37] Storment S, Scannell R, Shi P, Michael C, Pratt Q, Carter T and Rhodes T 2021 *Bulletin of the American Physical Society*

[38] Peebles W, Rhodes T, Hillesheim J, Zeng L and Wannberg C 2010 *Review of Scientific Instruments* **81** 10D902

[39] Lloyd B, Ahn J, Akers R, Appel L, Arends E, Axon K, Buttery R, Byrom C, Carolan P, Challis C *et al.* 2003 *Nuclear fusion* **43** 1665

[40] Piliya A and Popov A Y 2002 *Plasma physics and controlled fusion* **44** 467

[41] Gusakov E and Surkov A 2004 *Plasma physics and controlled fusion* **46** 1143

[42] Pereverzev G 1996 Paraxial wkb solution of a scalar wave equation *Reviews of Plasma Physics: Volume 19* ed Kadomtsev B (Springer) pp 1–48

[43] Pereverzev G 1998 *Physics of Plasmas* **5** 3529–3541

[44] Poli E, Peeters A and Pereverzev G 2001 *Computer Physics Communications* **136** 90–104

[45] Schekochihin A, Cowley S, Dorland W, Hammett G, Howes G G, Plunk G, Quataert E and Tatsuno T 2008 *Plasma Physics and Controlled Fusion* **50** 124024

[46] Schekochihin A, Cowley S, Dorland W, Hammett G, Howes G G, Quataert E and Tatsuno T 2009 *The Astrophysical Journal Supplement Series* **182** 310

[47] Barnes M, Parra F and Schekochihin A 2011 *Physical Review Letters* **107** 115003

[48] Lechte C 2009 *IEEE Transactions on Plasma Science* **37** 1099–1103

[49] Lechte C, Conway G, Görler T, Tröster-Schmid C *et al.* 2017 *Plasma Physics and Controlled Fusion* **59** 075006

[50] Bulanin V V and Yafanov M V 2006 *Plasma Physics Reports* **32** 47–55

[51] Ruiz Ruiz J, Parra F I, Hall-Chen V H, Christen N, Barnes B, Candy J, Garcia J, Giroud C, Guttenfelder W, Hillesheim J C, Holland C, Howard N T, Ren Y, White A E and JET contributors In press *Plasma Physics and Controlled Fusion*

[52] Lao L, John H S, Stambaugh R, Kellman A and Pfeiffer W 1985 *Nuclear fusion* **25** 1611

[53] Appel L, Huysmans G, Lao L, McCarthy P, Muir D, Solano E, Storrs J, Taylor D, Zwingmann W *et al.* 2006 A unified approach to equilibrium reconstruction *Proceedings-33rd EPS conference on Controlled Fusion and Plasma Physics, pp. P–2.160*

[54] Conway N, De Bock M, Michael C, Walsh M, Carolan P, Hawkes N, Rachlew E, McCone J, Shibaev S and Wearing G 2010 *Review of Scientific Instruments* **81** 10D738

[55] Scannell R, Walsh M, fdbsDunstan M, Figueiredo J, Naylor G, O'Gorman T, Shibaev S, Gibson K and Wilson H 2010 *Review of Scientific Instruments* **81** 10D520

[56] Welch P 1967 *IEEE Transactions on audio and electroacoustics* **15** 70–73

[57] Harris F J 1978 *Proceedings of the IEEE* **66** 51–83

[58] Happel T 2010 *Doppler Reflectometry in the TJ-II Stellarator: Design of an Optimized Doppler Reflectometer and its Application to Turbulence and Radial Electric Field Studies* Ph.D. thesis University Carlos III of Madrid

[59] Wen J, Shi Z, Zhong W, Liang A, Jiang M, Shi P, Yang C, Chen W, Fang K and Liu Z 2019 *Nuclear Fusion and Plasma Physics* **39** 1